Journal of Power Sources 412 (2019) 655–663

Contents lists available at ScienceDirect

Journal of Power Sources

journal homepage: www.elsevier.com/locate/jpowsour

High-mass loading electrodes with exceptional areal capacitance and cycling performance through a hierarchical network of MnO_2 nanoflakes and conducting polymer gel

Zhaokun Yang[a,b], Jun Ma[b,**], Sherif Araby[b], Dongjian Shi[a], Weifu Dong[a], Ting Tang[b], Mingqing Chen[a,*]

[a] Key Laboratory of Synthetic and Biological Colloids, Ministry of Education, School of Chemical and Material Engineering, Jiangnan University, Wuxi, 214122, PR China
[b] School of Engineering and Future Industries Institute, University of South Australia, Mawson Lakes, SA, 5095, Australia

HIGHLIGHTS

- A novel 3D hierarchical polyaniline/ MnO_2 composite network is developed.
- The network enables high MnO_2 mass loading of 7.3 mg cm^{-2}.
- It has the highest areal capacitance of 3516.7 mF cm^{-2}.
- It features 98.5% capacitance retention over 10,000 cycles.

GRAPHICAL ABSTRACT

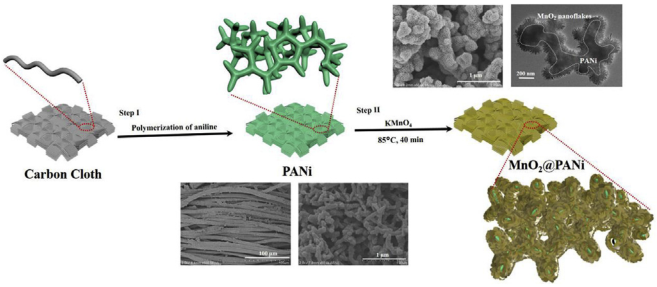

ARTICLE INFO

Keywords:
Three-dimensional networks
Conducting polymer gel
Manganese dioxide

ABSTRACT

Engineering electroactive materials onto 3D conductive scaffolds holds promise to the development of high-performance energy storage devices. In comparison with the existing scaffolds made of metals or carbon nanomaterials, we herein report a unique scaffold of 3D nanostructured polyaniline (PANi) network, where MnO_2 nanoflakes of 10 nm in thickness grow vertically to create a hierarchically structured composite. Through two simple sequential processes, a binder-free electrode with a high areal density of 8.3 mg cm^{-2} (7.3 for MnO_2 and 1.0 for PANi) is readily fabricated by using a piece of carbon cloth as the current collector. Measured with three-electrode configuration at 5 mV s^{-1}, the network delivers capacitance of 423.7 F g^{-1}, 3516.7 mF cm^{-2} and 106.6 F cm^{-3}, with retention of 98.5% over 10,000 cycles. The high capacitance especially areal capacitance is attributed to the maximum utilization of high-specific area MnO_2 nanoflakes through efficient electron and ion transfer which is enabled by two intimate interfaces respectively between MnO_2 and PANi and between PANi and carbon cloth. The superior cycling performance is mainly enabled by the volume-change accommodation of the hierarchically porous network. This composite network would provide a new methodology to maximize the electrochemical performance of metal oxides.

---

[*] Corresponding author.
[**] Corresponding author.
E-mail addresses: Jun.Ma@unisa.edu.au (J. Ma), mqchen@jiangnan.edu.cn (M. Chen).

https://doi.org/10.1016/j.jpowsour.2018.12.004
Received 16 April 2018; Received in revised form 28 November 2018; Accepted 2 December 2018

1. Introduction

Supercapacitors are one type of the most important storage devices for sustainable and renewable energy. Due to high power density and long cycle life, supercapacitors have a wide range of applications from portable electronics to hybrid electric vehicles to electric power grids [1–5]. It is urgent to improve the energy density of the existing supercapacitors without compromising power density and cycle life. The energy storage capability arises from two mechanisms, both occurring either at or near the electrode surface [2,3]. The first mechanism is electric double-layer capacitance [4,6], which refers to reversible ion adsorption-desorption at electrode surface or inside pores, being non-Faradaic processes. The second known as electrochemical capacitance is based on fast surface redox reactions, being Faradaic processes [3,7–9]. In comparison with double-layer capacitance of carbon materials (typically 90–300 $F\,g^{-1}$) [6,10,11], metal oxides or conducting polymers can deliver far higher peseudocapacitance (300–1200 $F\,g^{-1}$) and thus these have attracted increasing interests [8,12–15].

Manganese dioxide (MnO_2), storing charge via fast and reversible Faradaic reactions, is a typical electrochemical capacitive material (theoretical capacitance of $\sim$1380 $F\,g^{-1}$) due to abundance, low cost, and environmental friendliness [7,16,17]. Nevertheless, two significant challenges limit its practical applications: (i) poor electronic and ionic conductivity limits electrochemical performance at high charge/discharge rates [17–19], and (ii) rigid metal oxide nature often leads to structural collapse because of repetitive intercalation and removal of ions [20–22].

These challenges are usually addressed by three strategies:

(i) Synthesizing nanostructured MnO_2 (e.g. nanospheres [23], nanofibers [24], nanowires [25], nanoflakes [22,26], and nanoflowers [27]), which can both increase the accessible surface area to obtain high energy density and shorten the transport pathways for electrons and ions to attain high power density.

(ii) Either anchoring nanostructured MnO_2 onto conductive media, i.e. carbon nanotubes [28–30] and graphene [31–33], or coating with conducting polymers to fabricate composite particles for higher conductivity [34–37]. These composites have demonstrated substantial enhancement of specific capacitance due to synergy. Furthermore, conducting polymers usually have higher capacitance than neat carbon materials. Unfortunately, coating MnO_2 with conducting polymers prevented its full contact with electrolyte, restraining the utilization of MnO_2. Rather, loading MnO_2 onto the surface of conducting polymers to create composites proved more effective [22,38–41].

(iii) Directly depositing MnO_2 on 3D micro or nanostructured conductive substrates, to fabricate composite networks in the form of a freestanding film or sponge, such as carbon nanofiber paper [42], carbon cloth [16,18,43,44], Ni foam [45], 3D Ni skeleton [46], molybdenum carbide nanofibers [47], nanoporous gold [48] as well as graphene-based 3D conductive scaffolds [49–52]. This strategy (i) enables the maximal utilization of charge storage capability by providing direct contact between nano-sized MnO_2 and current collectors to enhance electron transport, and (ii) features high specific surface area, open-pore channels, and 3D micro or nanostructures with promising conductivity.

The first two strategies often relate to the conventional slurry coating process, where neither binder nor conductive additive have storage capability thus reducing specific capacitance. The third strategy can create binder-free scaffolds for electrodes, but unfortunately most scaffolds are fabricated from carbon materials or metals which are limited by low or no capacitance. Given that conductive, nanostructured scaffold proved highly effective in improving the electrochemical performance of active materials especially at high mass loading, a hypothesis made herein was that a 3D nanostructured conducting polymer scaffold would potentially enhance the capacitive performance of MnO_2 at high mass loading while retaining excellent cycling performance.

In this work, we report a two-step synthetic procedure where a piece of conductive carbon cloth is utilized as the substrate to carry a hierarchical network of MnO_2 nanoflake/3D porous nanostructured polyaniline (PANi). Initially formed on the cloth, PANi serves as 3D conductive network for the subsequent growth of MnO_2 nanoflakes. The hierarchical network not only offers high MnO_2 mass loading, but also provides (i) abundant PANi/MnO_2 interface and intimate electronic junction between PANi and carbon cloth for electron transfer, and (ii) sufficient interface between PANi, MnO_2 and electrolyte for ion transport. The electrode made of MnO_2/PANi network on the cloth delivers areal capacitance of 3516.7 $mF\,cm^{-2}$ and satisfactory cyclability with capacitance retention of 98.5% after 10,000 cycles.

2. Experimental

2.1. Preparation of 3D nanostructured PANi network

A 3D nanostructured PANi network was prepared on a piece of carbon cloth according to a ref. [53] In a typical process, solution A was made by mixing 45 μL of aniline (0.5 mmol), 135 μL of phytic acid solution (0.15 mmol) and 1 mL deionized water. Then 70 mg of ammonium persulfate (0.3 mmol) was dissolved in 0.5 mL deionized water to form solution B. After these two batches of solution were cooled to 4 °C in a refrigerator, they were rapidly mixed and immediately dropped onto the cloth (coating area 1 × 1 cm). The cloth was held at 4 °C for 8 h to complete polymerization, followed by washing with ethanol to remove both by-product aniline oligomer and excess phytic acid. The mass loading of PANi on carbon cloth was controlled at $1.0 \pm 0.1\,mg\,cm^{-2}$ (see details in the Supporting Information).

2.2. Coating PANi network with MnO_2 nanoflakes (MnO_2/PANi network)

A piece of carbon cloth coated with PANi network was soaked into 50 mL of aqueous solution containing 0.79 g of $KMnO_4$ (5 mmol) and 265 μL of H_2SO_4. Then they were placed in a water bath and heated to 85 °C. By trial and error, reaction time was controlled at 40 min to attain a balance between the formation of MnO_2 nanoflakes and the structural integrity of PANi. The as-prepared samples were then washed with distilled water and naturally dried. For comparison, MnO_2 nanoflakes directly grown on carbon cloth were prepared by immersing a piece of carbon cloth into the above reaction system for the same reaction time. The mass loading of active materials was measured by a high precision balance (0.001 mg) following each synthesis step. The mass loadings of MnO_2 on the network and on the cloth are 7.3 ± 0.5 and $1.2 \pm 0.2\,mg\,cm^{-2}$, respectively.

2.3. Characterization

Morphology was examined by field emission scanning electron microscopy (SEM, Hitachi, S-4800) and transmission electron microscopy (TEM, JEOL, JEM-2100). The crystal structure was investigated by X-ray diffractometer (XRD, D8 Advance, Bruker) with Cu *Kα* radiation (λ = 1.5418 Å). Raman spectra were recorded on a Renishaw Raman spectrometer excited with a 532 nm He-Ne laser.

2.4. Electrochemical measurement

The methodology for characterizing the electrode materials of supercapacitors is not well standardized in academia. Meryl et al. commented that some configuration, such as testing fixture type, the mass of materials, and the thickness of electrode, would pose great influence on the testing outcomes [54]. While two-electrode-configuration relates more closely to the performance of a commercial packaged cell, three-electrode-configuration would be more appropriate to accurately evaluate the electrochemical performance of electrode materials [54–56]. Since the mass loading of a typical industrial porous carbon electrode is at about 10 mg cm^{-2} [57], a laboratory electrode should have comparable mass loading — extremely low mass loading often exaggerates the electrode performance [54].

In this research we designed and fabricated composite electrodes by using carbon cloth as the current collector; each electrode had mass loading of 8.3 mg cm^{-2} (7.3 mg cm^{-2} for MnO_2 and 1.0 mg cm^{-2} for PANi). The electrode thickness after loading active materials was measured to be 0.33 mm, which showed negligence increase in comparison with that of carbon cloth (0.32 mm). All electrochemical measurements of individual electrodes were conducted in 1.0 M aqueous Na_2SO_4 solution using a standard three-electrode system with a platinum plate counter electrode and a saturated calomel electrode as the reference electrode. Cyclic voltammetry, electrochemical impedance spectroscopy, and galvanostatic charge/discharge measurements were performed by an electrochemical workstation. The specific capacitance (C_{sp}, F g^{-1}) was calculated from CV curves and discharge curves according to the following equations:

$$C_{sp} = \frac{\int I(V)dV}{\nu \times m \times \Delta V} \tag{1}$$

$$C_{sp} = \frac{I \times \Delta t}{m \times \Delta V} \tag{2}$$

Where I (A) is the current, ΔV (V) is the potential window, ν (mV s^{-1}) is the potential scan rate, m (g) is the mass of the electroactive materials in the electrodes, and Δt (s) is the discharge time.

For portable and miniature devices, both volumetric and areal capacitance are more important than gravimetric capacitance [50]. Thus, gravimetric and areal capacitance were calculated in this work by the total mass of electrode materials – PANi and MnO_2. Volumetric capacitance was calculated by the volume of the entire electrode including PANi, MnO_2, and the current collector – carbon cloth.

3. Results and discussion

Previous studies [22,34–41,58] reported strong synergy between MnO_2 and conducting polymers for capacitive performance. However, most of these studies utilized MnO_2 as a core surrounded by a shell of conducting polymers which prevented the core from sufficiently contacting electrolyte. The problem is addressed herein by anchoring MnO_2 onto the 3D nanostructured PANi network on carbon cloth, to form a novel MnO_2/PANi network; the strategy enables direct contact between MnO_2 and electrolyte, provides continuous electronic conducting network, and shortens transport pathways for electrolyte ions; thus it holds great potential to improve capacitive performance.

Our strategy consists of two steps as illustrated in Fig. 1.

Step I: Synthesis of a 3D nanostructured PANi network on a piece of carbon cloth via simple polymerization. The PANi network formed by the crosslinking of phytic acid behaves like adhesive, so it firmly adheres to carbon cloth creating a mechanically strong electronic junction.

Step II: The vertical growth of MnO_2 nanoflakes on the network, via two steps: (i) forming MnO_2 seeds by soaking the network in $KMnO_4$ solution and (ii) turning the seeds into nanoflakes by soaking at 85 °C for 30–50 min.

Fig. 2a–c contain low-magnification SEM micrographs of carbon cloth, PANi, and the MnO_2/PANi network. In this work, carbon cloth is served as the skeleton for forming a porous, interconnected network, as shown in Fig. S1. The network is composed of dendritic PANi nanofibers (Fig. 2d) having a diameter of 80 ± 5 nm, and these fibers are intimately connected to carbon cloth by a thin PANi layer (30–50 nm in thickness) (Fig. 2e). The layer should provide ideal electrical connection between the fibre and the network. Fig. 2c exhibits that the network is grown over the entire skeleton of the cloth. Specifically, MnO_2 nanoflakes each of 10 ± 0.5 nm in thickness (shown in the insert micrograph of Fig. 2f) are vertically anchored onto the PANi nanofibers, forming unique structure where the nanofiber is a core and the nanoflakes are the shell (Fig. 2h). Through loading MnO_2 nanoflakes, the nanofiber diameter increases from 80 to 150 nm, as demonstrated by the double-headed arrows in Fig. 2d and f. TEM micrographs (Fig. 2g and h) confirm the size and conformation of the PANi nanofibers and the composite network.

The structural hierarchy is clearly seen by SEM and TEM. This composite network contains 3D topologies from nano to microscale. On the nanoscale, the network is comprised of MnO_2 nanoflakes (each ~10 nm in thickness) on PANi nanofibers (~80 nm in diameter) as well as the nanopores (blue arrows in Fig. 2f inset) between vertically aligned nanoflakes. On the microscale, this network is characterized by micron-sized pores marked by the orange-colour arrows in Fig. 2f. In addition, carbon cloth (Fig. 2a) consists of micron-sized fibers of 10 μm in diameter and interspace of 10–30 μm.

The hierarchical network would provide large accessible electroactive surface areas, maximizing the energy storage capability of MnO_2. In the meantime, this network enabled high MnO_2 mass loading of 7.3 mg cm^{-2}, which would significantly improve the areal capacitance. Although loading MnO_2 onto the surface of conducting polymer fibers has been reported [22,38–40], our work represents a giant step forward by building up a 3D hierarchical conducting polymer network which takes a high loading of MnO_2 nanoflakes.

Different crystallographic phases endow MnO_2 with different capacitance [16,59]. XRD patterns of MnO_2 nanoflakes and MnO_2/PANi network were analyzed to identify their crystal phases (Fig. 3a). Obvious diffraction patterns are seen at 2θ of ~26°, 36.3°, and 65.2°, illustrating the formation of Birnessite-type δ-MnO_2 (JCPDS#42–1317). Although the diffraction at ~26° is contributed by both δ-MnO_2 and carbon cloth substrate [60], the formation of Birnessite-type δ-MnO_2 is evidenced by others. A broad pattern at ~25.4° is ascribed to the π-π stacking-induced, partial periodicity arrangement of PANi chains, which was reported for high electrical conductivity [53]; noteworthy is that neat PANi powder was measured in this case. Previous studies have shown that δ-MnO_2 is able to deliver the highest capacitance of all types of MnO_2, because of its 2D stacked structure with atomic tunnels of 0.7 nm [16,59]. Moreover, the structure may facilitates the formation of MnO_2 nanoflakes [22].

We further verified the co-existence of MnO_2 and PANi with Raman spectroscopy (Fig. 3b) and Energy Dispersive X-ray (EDX) analysis (Fig. 3c). In Fig. 3c, N element from PANi and Mn and O from MnO_2 are both found to uniformly distribute across the samples. In this work, Raman spectra were obtained by using blue excitation line (532 nm) of laser due to its effectiveness on PANi [61]. By trial and error, we used 0.5% of excitation laser power to collect the Raman spectrum of MnO_2 due to its instability and low Raman response [62,63]. For MnO_2/PANi, laser power was set at 1.0% to alleviate PANi-induced suppression. For MnO_2/PANi, Raman bands at 159, 516, 597, and 676 cm^{-1} correspond to MnO_2 [16,49]. The presence of PANi is supported by characteristic peaks at 1165 cm^{-1} (C–H bending of benzenoid rings), 1494 cm^{-1} (C=N stretching of the quinoid rings), and 1595 cm^{-1} (C–C stretching of benzenoid rings) [61,64,65]. Specifically, two distinct peaks at 1325 and 1395 cm^{-1} (C–N^{+} fragment-stretching vibrations) indicate the formation of a highly electronically conducting emeraldine salt [61,64,65], which would provide fast electron transport for MnO_2 nanoflakes, corresponding to our later discussion for electrochemical impedance spectra.

The electrochemical performance of MnO_2 nanoflakes and MnO_2/PANi network was tested by a three-electrode system using 1.0 M Na_2SO_4 electrolyte. The electrodes of both materials show quasi-rectangular-shaped cyclic voltammetry (CV) curves at scan rates of 5–150 mV s^{-1} (Fig. 4a and b), whilst distortion is seen with increase in scan rate. Albeit redox peaks being nearly indistinguishable in the CV

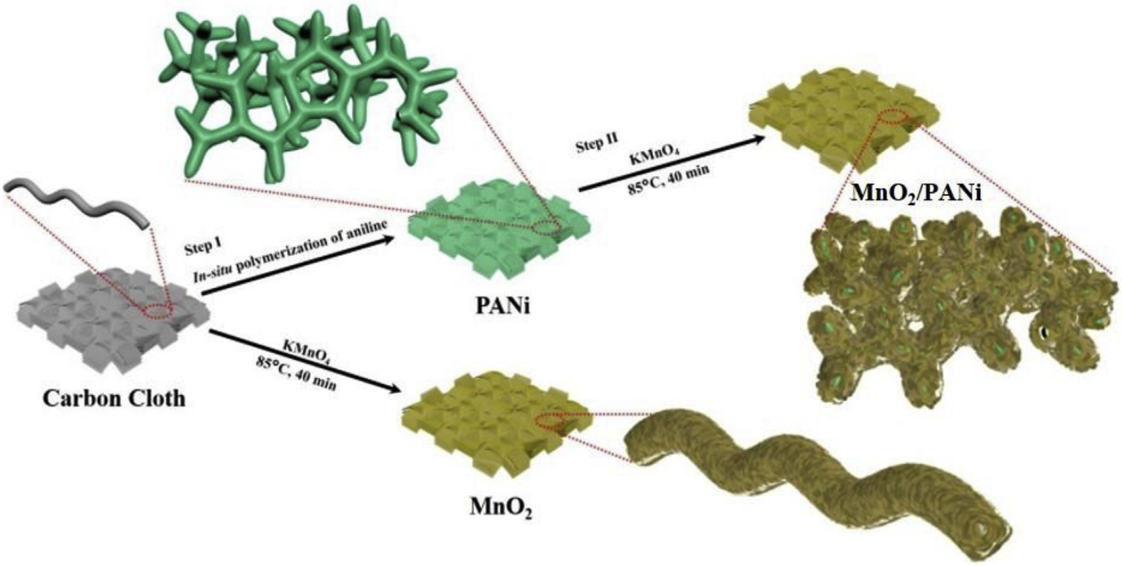

Fig. 1. Schematics for the fabrication of MnO_2/PANi network through Step I & II, and for the formation of MnO_2 nanoflakes directly on carbon cloth.

curves, reversible Faradaic reactions occurred, which involved the surface adsorption/desorption and intercalation/de-intercalation processes of Na^+ into MnO_2 nanoflakes and the reversible doping/de-doping of SO_4^{2-} anions into PANi [8,22]:

$$MnO_2 + xNa^+ + xe^- \leftrightarrow MnOONa_x$$

$$PANi^{n+}[SO_4^{2-}]_n + ne^- \leftrightarrow PANi^0 + nSO_4^{2-}$$

The intercalation/de-intercalation process during the reversible Faradaic redox reaction of pseudocapacitive materials has been recently proposed for some pseudocapacitive materials [66–68], including MnO_2 [2,3,54,56]. However, mechanisms are still not quite clear. From

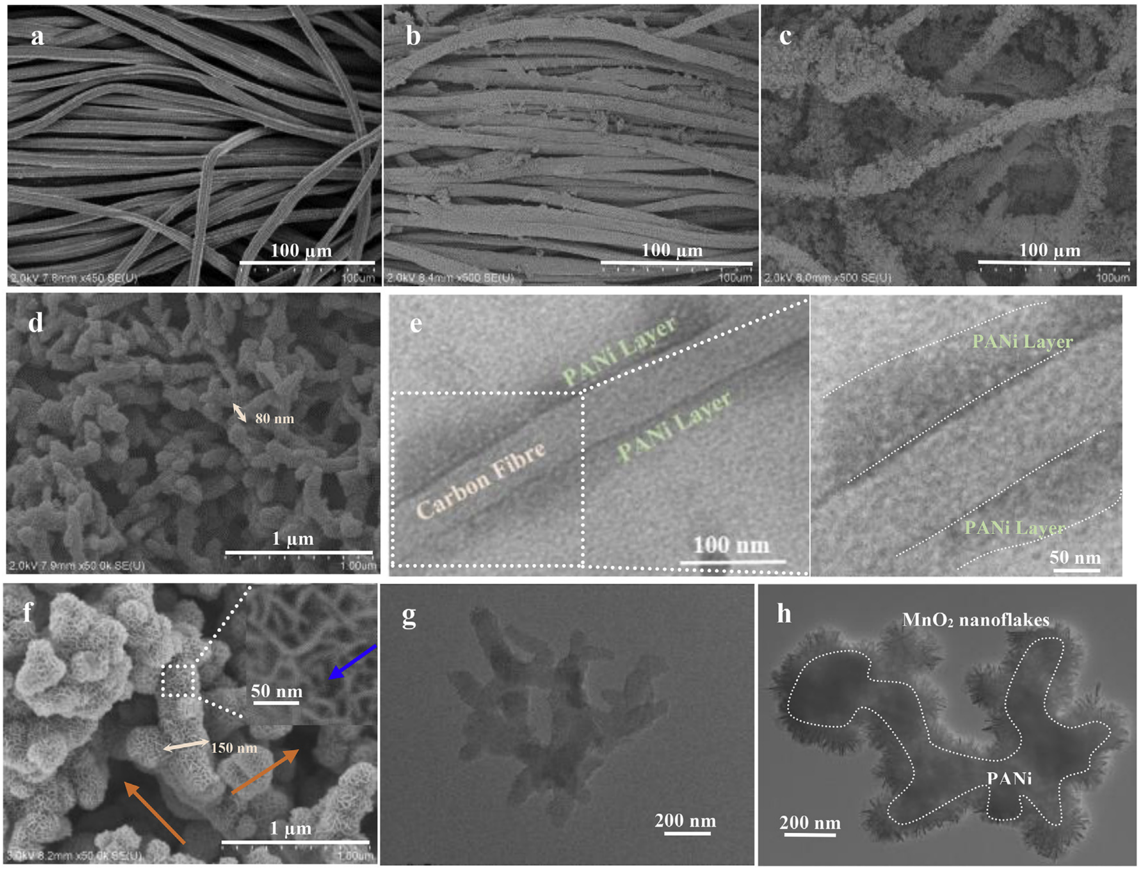

Fig. 2. SEM micrographs of (a) carbon cloth, (b & d) PANi network on the cloth, and (c & f) MnO_2 nanoflakes grown on PANi network on the cloth. TEM micrograph of (e) the interface between PANI and carbon fibre, (g) PANi, and (h) MnO_2/PANi network. Fig. 2f inset shows MnO_2 nanoflakes of 10 ± 0.5 nm in thickness. Blue arrow and orange arrows in Fig. 2f denote nanopores and micropores in network, respectively. (For interpretation of the references to colour in this figure legend, the reader is referred to the Web version of this article.)

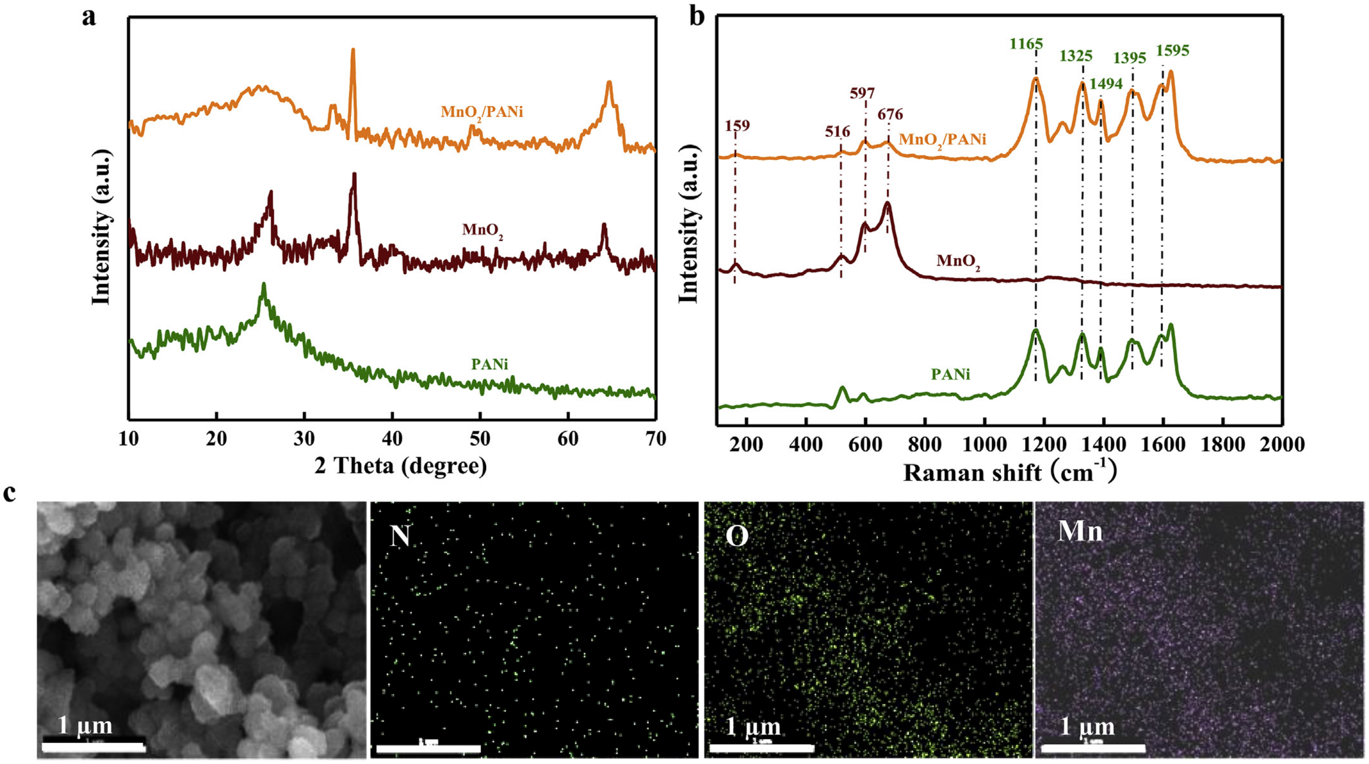

Fig. 3. (a) XRD patterns and (b) Raman spectra of PANi, MnO_2 nanoflakes, and MnO_2/PANi network. (c) EDX elemental mapping of MnO_2/PANi network.

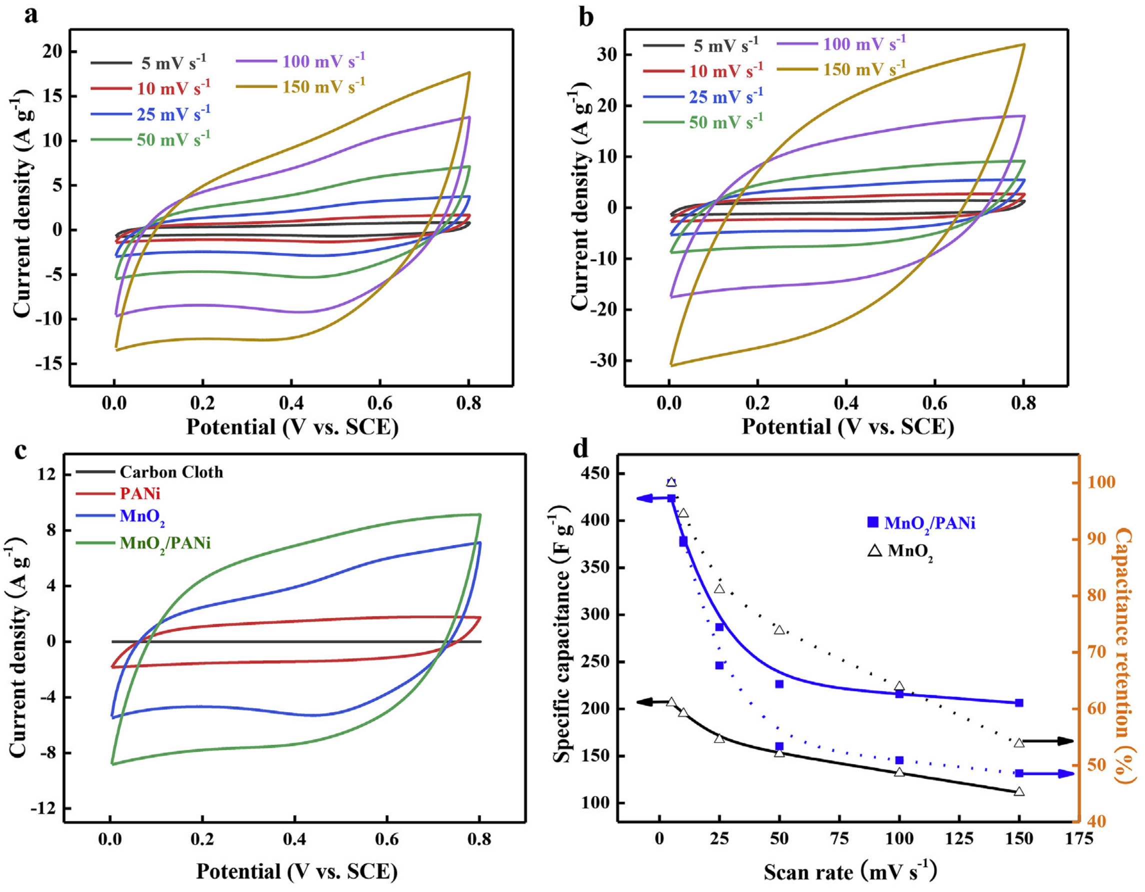

Fig. 4. CV curves of (a) MnO_2 nanoflakes and (b) MnO_2/PANi network. (c) CV curves of carbon cloth, PANi, MnO_2 nanoflakes, and MnO_2/PANi network at 50 mV s^{-1}. (d) Specific capacitance and capacitance retention of MnO_2 nanoflakes and MnO_2/PANi network calculated from CV curves.

our understanding, the continuous change of x during Na^+ intercalation/de-intercalation processes might result in the nearly identical current response over the entire potential, likely leading to nearly rectangular CVs. Further research is needed to fully understand the mechanisms.

The distortion of CV curves represents the electrode polarization. Especially a curve in Fig. 4b showing the largest distortion should be caused by relatively sluggish electron transfer at high scan rate of $150\,mV\,s^{-1}$. In alignment with most literature, this study selected $150\,mV\,s^{-1}$ as the highest scan rate, and the testing outcome shows competitiveness of our electrode materials in comparison with those reported MnO_2 based electrodes [18,22,27,38,46,69]. We anticipate that conductive polymer scaffolds with higher electronic conductivity (such as PEDOT) would be extensively investigated to further improve the performance at high scan rates.

Fig. 4c contains CV curves of MnO_2 nanoflakes, PANi network, and MnO_2/PANi network at $50\,mV\,s^{-1}$. The highest charge storage is seen for MnO_2/PANi network. Fig. 4d displays the specific capacitance of MnO_2 nanoflakes and MnO_2/PANi network calculated from their CV curves. The network shows far higher capacitance at all scan rates 5–$150\,mV\,s^{-1}$). The highest specific capacitance reaches $423.7\,F\,g^{-1}$ at $5\,mV\,s^{-1}$, which doubles that of MnO_2 nanoflakes ($206.5\,F\,g^{-1}$).

To further evaluate the electrochemical capacitive performance of MnO_2/PANi network, galvanostatic charge/discharge (GCD) curves at various current densities are collected in Fig. S3a&b. The triangular curves demonstrate an ideal capacitive behavior. The long discharge time of the network indicates higher capacitance than MnO_2 nanoflakes at $1\,A\,g^{-1}$ (Fig. S3c). Fig. S3d exhibits the relationship between specific capacitance and current density. The improvement of specific capacitance occurs at all current densities, in agreement with the CV analysis. MnO_2/PANi network delivers an ultrahigh areal capacitance of $3516.7\,mF\,cm^{-2}$ at $5\,mV\,s^{-1}$, whereas MnO_2 nanoflakes only show an areal capacitance of $247.8\,mF\,cm^{-2}$. It translates to volumetric capacitance of $106.6\,F\,cm^{-3}$ by calculating the volume of the entire electrode including the current collector. The network structure design exhibits capacitance retention of 48.7% at $150\,mV\,s^{-1}$ (Fig. S3d), which is slightly lower than that (53.9%) of MnO_2 nanoflakes directly grown on carbon cloth. However, the network electrode shows a higher specific capacitance value (206.3 versus $111.3\,F\,g^{-1}$). Of previously reported MnO_2 based composite electrodes, our MnO_2/PANi network exhibits the highest areal capacitance and relatively high specific capacitance, and more importantly, it features high mass loading (Table 1).

It is known that high mass loading often pairs with low specific capacitance. However, this is not a problem in the current research, where the 3D composite network not only enabled high mass loading of $8.3\,mg\,cm^{-2}$ ($7.3\,mg\,cm^{-2}$ of MnO_2 and $1.0\,mg\,cm^{-2}$ of PANi) but provided efficient electron/ion transport pathways. The mass loading was made by trial and errors, as higher loading needs longer reaction time and it proved to damage the network. Fig. S4 contains SEM micrographs of the as-prepared MnO_2/PANi network with different reaction time (30–50 min). Unnecessarily long reaction time proved to damage the network, and it likely caused the aggregation of the nanoflakes (Fig. S4c), because PANi was consumed as a reducing agent for the nanoflakes growth; superfluous PANi dissolved in solution would form new reduction sites leading to aggregation of the nanoflakes. Therefore, the reaction time was selected as 40 min, which is supported by the low electrochemical performance for reaction time of 50 min (sample denoted MnO_2/PANi-50).

Fig. S5a & b show the electrochemical performance of the composite network prepared with 50-min reaction time (MnO_2/PANi-50). Although quasi-rectangular-shaped CV curves and triangular GCD curves are observed, the specific capacitance of MnO_2/PANi-50 is significantly lower (Fig. 5a). MnO_2/PANi-30 delivers comparative specific capacitance with MnO_2/PANi-40 at different scanning rates (Fig. 5a), but its areal capacitance is lower than that of MnO_2/PANi-40 (Fig. S5c & d) due to low mass loading (4.8 versus $7.3\,mg\,cm^{-2}$). Areal capacitance is one of the most important performance metrics in practice owing to limited footprint area.

This study addressed the poor cycling performance of the MnO_2/conducting polymer composite electrodes [22,71]. The network electrode of MnO_2/PANi-40 shows 98.5% capacitance retention after 10,000 cycles (Fig. 5c), demonstrating ultrahigh electrochemical durability in comparison with 86.2% for MnO_2 electrode. Interestingly, the specific capacitance of both samples exhibits a slight increase (capacitance retention $>$ 100%) within the first 1200 cycles (Fig. 5c). The increase may be ascribed to the activation effect (Na^+ intercalation) of MnO_2 nanoflakes. Some reports have shown that the pre-insertion of cations (such as Na^+ and K^+) into MnO_2 can induce Mn^{3+}/Mn^{4+} redox couple thus increasing the capacitance [69,72]. This explains why MnO_2 electrode delivered a higher increment than MnO_2/PANi network. However, the insertion must have resulted in the excessive expansion of the electrode, thus inducing poor cycling stability for the MnO_2 electrode. Such an expansion in this study was much alleviated by the accommodation effect of the hierarchically porous, interconnected MnO_2/PANi network. The superior cycling performance can be visualized by the structural difference between the as-prepared electrodes and the cycled electrodes. Fig. S6 exhibits SEM micrographs

Table 1

Comparison of specific capacitance, areal capacitance, and volumetric capacitance of MnO_2 based electrodes.

Electrode	Test configuration	Mass loading (mg cm^{-2})	Areal Capacitance (mF cm^{-2})	Volumetric capacitance (F cm^{-3})	Specific Capacitance (F g^{-1})
Graphene-MnO_2 [31]	two-electrode	unknown	800 at $1\,mV\,s^{-1}$	203 at $1\,mV\,s^{-1}$	1145 at $1\,mV\,s^{-1}$
Graphene-MnO_2 [49]	two-electrode	9.8	1420 at $2\,mV\,s^{-1}$	71 at $2\,mV\,s^{-1}$ (Calculated)	145 at $2\,mV\,s^{-1}$ (Calculated)
Graphene/PEDOT/MnO_2 [32]	two-electrode	unknown	unknown	unknown	866.11 at $20\,mV\,s^{-1}$
CNT-MnO_2 [29]	threee-electrode	8.3	2800 at $0.05\,mV\,s^{-1}$	unknown	337.4 at $0.05\,mV\,s^{-1}$
CNT-MnO_2 [28]	threee-electrode	1.97	293 at $0.2\,A\,g^{-1}$	177.5 at $0.2\,A\,g^{-1}$	149 at $0.2\,A\,g^{-1}$
CNT@PPy@MnO_2 [39]	threee-electrode	unknown	unknown	16.1 at $2\,mV\,s^{-1}$	325 at $2\,mV\,s^{-1}$
MnO_2/3D Ni [46]	threee-electrode	unknown	unknown	unknown	1250 at $10\,A\,g^{-1}$
H-TiO_2@MnO_2 [43]	threee-electrode	0.2	85.4 at $10\,mV\,s^{-1}$ (Calculated)	unknown	449.6 at $10\,mV\,s^{-1}$
porous carbon-MnO_2 [70]	threee-electrode	6.5	1500 at $2\,mV\,s^{-1}$	90 at $2\,mV\,s^{-1}$	230 at $2\,mV\,s^{-1}$
Nanoporous gold/MnO_2 [48]	two-electrode	unknown	unknown	unknown	1145 at $50\,mV\,s^{-1}$
PPy covered MnO_2 [36]	threee-electrode	14	1982.4 at $2\,mA\,cm^{-2}$ (Calculated)	unknown	141.6 at $2\,mA\,cm^{-2}$
PANi covered MnO_2 [37]	threee-electrode	3	759 at $2\,mV\,s^{-1}$ (Calculated)	unknown	253 at $2\,mV\,s^{-1}$
MnO_2@PANi [38]	threee-electrode	0.8	306.4 at $0.5\,A\,g^{-1}$ (Calculated)	unknown	383 at $0.5\,A\,g^{-1}$
MnO_2@PPy [22]	threee-electrode	1	276 at $2\,A\,g^{-1}$	unknown	276 at $2\,A\,g^{-1}$
This work	threee-electrode	8.3	3516.7 at $5\,mV\,s^{-1}$	106.6 at $5\,mV\,s^{-1}$	423.7 at $5\,mV\,s^{-1}$
MnO_2/PANI network			3883.5 at $1\,A\,g^{-1}$	117.7 at $1\,A\,g^{-1}$	467.9 at $1\,A\,g^{-1}$

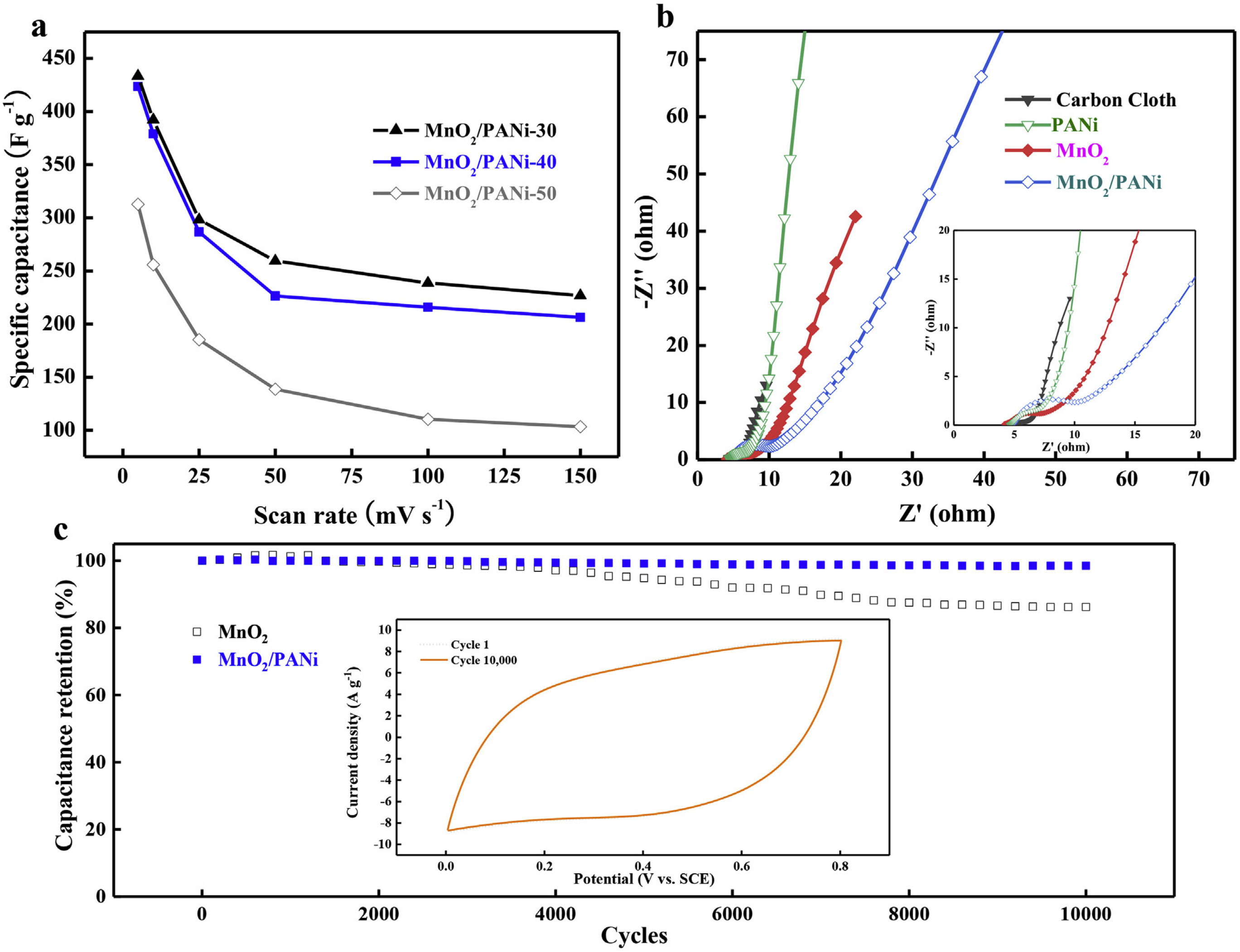

Fig. 5. (a) Specific capacitance of MnO_2/PANi with different reaction time calculated from CV curves. (b) Nyquist plots of carbon cloth, PANi, MnO_2 nanoflakes, and MnO_2/PANi network. The inset is the enlarged Nyquist plot from the high-frequency region. (c) Cycling performance of MnO_2 nanoflakes and MnO_2/PANi network at 50 mV s^{-1} for 10,000 cycles. The inset shows CV curves of the first and the 10,000th cycle for MnO_2/PANi network.

of the cycled electrodes of (i) MnO_2/PANi network and (ii) MnO_2 on cloth. In comparison with the structure shown in Fig. 4f, the hierarchical architecture maintains well where the vertically alignment of MnO_2 nanoflakes remains barely changed in the composite (Fig. S6a), and the cycled MnO_2 on cloth has obviously collapsed (as circled in Fig. S6b) in comparison with the well aligned MnO_2 nanoflakes prior to the testing in Fig. S2.

Although the hierarchical network has delivered remarkable electrochemical performance, its mechanical strength needs further improvement which may lead to further higher cycling performance. Future research should focus on the development of new conducting polymer networks having not only excellent electrochemical performance but mechanical robustness.

To understand the high specific capacitance and cycling performance, electrochemical impedance spectroscopy (EIS) was conducted between 100 kHz and 0.01 Hz at open-circuit voltage. Fig. 5b shows Nyquist plots for carbon cloth, MnO_2 nanoflakes, PANi network, and the MnO_2/PANi network on carbon cloth. A reasonable equivalent circuit model (Fig. S7), which consists of equivalent series resistance (R_s), charge transfer resistance (R_{ct}), Warburg diffusion resistance (W), double-layer capacitance (C_{dl}), and limit capacitance (C_L), was used to obtain the following data from the software ZsimpWin [18,73]. The R_s for MnO_2 nanoflakes and MnO_2/PANi network are 4.716 and 4.922 Ω, respectively; such low resistance values were anticipated because no binder was used; these imply fast charge transfer and favorable ion transport through the entire electrode. The nearly identical R_s values suggest that the incorporation of PANi network on carbon cloth should impede neither charge transfer nor ion transport. The ultralow value of Warburg type element (W), which relates to electrolyte ions diffusion, implies fast ion transport in the electrodes [73,74]. The fast kinetics for both ions and electrons are provided by both hierarchically porous channels and continuous electron transfer pathways enabled by the rationally designed composite network.

The R_{ct} of MnO_2 grown directly on carbon cloth was found to be 10.058 Ω, but the addition of PANi network slightly increased it to 12.193 Ω. The change of R_{ct} is unexpected, because we anticipated that the incorporation of conductive PANi into MnO_2 should improve the composite conductivity. This arises from the high mass loading of MnO_2 enabled by the network. It should note that only 1.2 mg cm^{-2} of MnO_2 was loaded onto the cloth, resulting in R_{ct} of 10.058 Ω. However, in the latter case 1.0 mg cm^{-2} of PANi enabled high loading of MnO_2–7.3 mg cm^{-2}; the resistance reduction caused by such a high MnO_2 loading should overshadow the increase caused by such a low quantity of PANi.

The calculated C_{dl} and C_L from EIS are given in Fig. S7. Through incorporating PANi network, C_{dl} increases from 23.87 to 150.28 F g^{-1}

and the C_L increases from 525.1 to 783.6 F g^{-1}. The enhancement of C_{dl} is mainly caused by high surface area of the hierarchically porous network. C_L refers to the intrinsic capacitance of the electrode assuming that the entire surface area is active [18,73,75]. Although this study enables C_L of 783.6 F g^{-1}, there is still a long way to reach the theoretical value (1380 F g^{-1}) of MnO_2. From our perspectives, further improvement can be made by exploring synergy and optimizing structure design.

Overall, the improvement of capacitive performance is ascribed to the following compositional and structural features.

- The porous nanostructured PANi network provides abundant surface where MnO_2 nanoflakes grow, allowing large mass loading which creates high areal capacitance,
- Vertically aligned MnO_2 nanoflakes having nanosized channels may provide abundant interfaces with electrolyte, in favor of fast diffusion of electrolyte ions,
- Rapid electronic transport is promoted by the intimate electronic junction contact between carbon cloth, PANi, and MnO_2 as well as the continuous polymer network,
- Strong synergy of PANi and MnO_2 towards high capacitive performance,
- Hierarchically porous network can accommodate the volume change of PANi and MnO_2 during charge/discharge processes.

4. Conclusions

In summary, a hierarchical MnO_2/PANi network on carbon cloth has been developed through a two-step procedure: (i) polymerization of aniline towards 3D nanostructured PANi network on the cloth and (ii) vertical growth of MnO_2 nanoflakes on the network. The network acting as the scaffold provided not only abundant PANi/MnO_2 interfaces for enhanced electronic transport but interconnected porous network that accommodated the volume change of PANi and MnO_2 during charge/discharge processes. MnO_2 nanoflakes vertically grown on PANi nanofibers provided large accessible electroactive surface area. The resulting composite network delivered ultrahigh areal capacitance of 3516.7 mF cm^{-2} and excellent cycling stability – 98.5% capacitance retention over 10,000 cycles. This work may open up a new avenue to improve the electrochemical performance of metal oxides as a binder-free electrode for supercapacitors.

Acknowledgements

This work was funded by the National Nature Science Foundation of China (Grant No. 21571084), Postgraduate Research & Practice Innovation Program of Jiangsu Province (KYCX17_1433) and MOE & SAFEA for the 111 Project (B13025). JM acknowledges the financial support from the Australian Research Council (IH150100003). JM appreciates technical support provided by L O'Donovan and A Netting at Adelaide Microscopy.

Appendix A. Supplementary data

Supplementary data to this article can be found online at https://doi.org/10.1016/j.jpowsour.2018.12.004.

References

[1] G.P. Wang, L. Zhang, J.J. Zhang, Chem. Soc. Rev. 41 (2012) 797–828.
[2] M.R. Lukatskaya, B. Dunn, Y. Gogotsi, Nat. Commun. 7 (2016) 12647–12659.
[3] P. Simon, Y. Gogotsi, Nat. Mater. 7 (2008) 845–854.
[4] J.R. Miller, P. Simon, Science 321 (2008) 651–652.
[5] L. Li, Z. Lou, D. Chen, K. Jiang, W. Han, G. Shen, Small (2017) 1702829–1702851.
[6] L.L. Zhang, X.S. Zhao, Chem. Soc. Rev. 38 (2009) 2520–2531.
[7] W.F. Wei, X.W. Cui, W.X. Chen, D.G. Ivey, Chem. Soc. Rev. 40 (2011) 1697–1721.
[8] A.M. Bryan, L.M. Santino, Y. Lu, S. Acharya, J.M. D'Arcy, Chem. Mater. 28 (2016) 5989–5998.
[9] Z. Yang, A. Qiu, J. Ma, M. Chen, Compos. Sci. Technol. 156 (2018) 231–237.
[10] Z. Chen, Y. Qin, D. Weng, Q. Xiao, Y. Peng, X. Wang, H. Li, F. Wei, Y. Lu, Adv. Funct. Mater. 19 (2009) 3420–3426.
[11] M. Inagaki, H. Konno, O. Tanaike, J. Power Sources 195 (2010) 7880–7903.
[12] G. Yu, L. Hu, M. Vosgueritchian, H. Wang, X. Xie, J.R. McDonough, X. Cui, Y. Cui, Z. Bao, Nano Lett. 11 (2011) 2905–2911.
[13] M. Moussa, Z. Zhao, M.F. El-Kady, H. Liu, A. Michelmore, N. Kawashima, P. Majewski, J. Ma, J. Mater. Chem. 3 (2015) 15668–15674.
[14] J. Cao, X. Li, Y. Wang, F.C. Walsh, J.-H. Ouyang, D. Jia, Y. Zhou, J. Power Sources 293 (2015) 657–674.
[15] Z. Yang, L. Tang, J. Ye, D. Shi, S. Liu, M. Chen, Electrochim. Acta 269 (2018) 21–29.
[16] C. Zhu, L. Yang, J.K. Seo, X. Zhang, S. Wang, J. Shin, D. Chao, H. Zhang, Y.S. Meng, H.J. Fan, Materials Horizons 4 (2017) 415–422.
[17] Y. Song, T. Liu, B. Yao, M. Li, T. Kou, Z.-H. Huang, D.-Y. Feng, F. Wang, Y. Tong, X.-X. Liu, ACS Energy Letters 2 (2017) 1752–1759.
[18] T. Zhai, S. Xie, M. Yu, P. Fang, C. Liang, X. Lu, Y. Tong, Nanomater. Energy 8 (2014) 255–263.
[19] M. Toupin, T. Brousse, D. Bélanger, Chem. Mater. 16 (2004) 3184–3190.
[20] L. Dong, C. Xu, Y. Li, C. Wu, B. Jiang, Q. Yang, E. Zhou, F. Kang, Q.H. Yang, Adv. Mater. 28 (2016) 1675–1681.
[21] J. Yue, X. Gu, X. Jiang, L. Chen, N. Wang, J. Yang, X. Ma, Electrochim. Acta 182 (2015) 676–681.
[22] W. He, C. Wang, F. Zhuge, X. Deng, X. Xu, T. Zhai, Nanomater. Energy 35 (2017) 242–250.
[23] Y. Zhao, Y. Meng, P. Jiang, J. Power Sources 259 (2014) 219–226.
[24] H.Y. Wang, F.X. Xiao, L. Yu, B. Liu, X.W.D. Lou, Small 10 (2014) 3181–3186.
[25] Z. Lv, Y. Luo, Y. Tang, J. Wei, Z. Zhu, X. Zhou, W. Li, Y. Zeng, W. Zhang, Y. Zhang, Adv. Mater. 30 (2018) 1704531–1704539.
[26] P. Sun, H. Yi, T. Peng, Y. Jing, R. Wang, H. Wang, X. Wang, J. Power Sources 341 (2017) 27–35.
[27] L. Wu, L. Hao, B. Pang, G. Wang, Y. Zhang, X. Li, J. Mater. Chem. 5 (2017) 4629–4637.
[28] P. Wu, S. Cheng, L. Yang, Z. Lin, X. Gui, X. Ou, J. Zhou, M. Yao, M. Wang, Y. Zhu, Acs Appl Mater Inter 8 (2016) 23721–23728.
[29] L. Hu, W. Chen, X. Xie, N. Liu, Y. Yang, H. Wu, Y. Yao, M. Pasta, H.N. Alshareef, Y. Cui, ACS Nano 5 (2011) 8904–8913.
[30] K. Wang, S. Gao, Z. Du, A. Yuan, W. Lu, L. Chen, J. Power Sources 305 (2016) 30–36.
[31] M.F. El-Kady, M. Ihns, M. Li, J.Y. Hwang, M.F. Mousavi, L. Chaney, A.T. Lech, R.B. Kaner, Proc. Natl. Acad. Sci. Unit. States Am. 112 (2015) 4233–4238.
[32] M. Moussa, G. Shi, H. Wu, Z. Zhao, N.H. Voelcker, D. Losic, J. Ma, Mater. Des. 125 (2017) 1–10.
[33] W. Ma, S. Chen, S. Yang, W. Chen, Y. Cheng, Y. Guo, S. Peng, S. Ramakrishna, M. Zhu, J. Power Sources 306 (2016) 481–488.
[34] R. Liu, S.B. Lee, J. Am. Chem. Soc. 130 (2008) 2942–2943.
[35] W. Xiao, J.S. Chen, Q. Lu, X.W. Lou, J. Phys. Chem. C 114 (2010) 12048–12051.
[36] A. Bahloul, B. Nessark, E. Briot, H. Groult, A. Mauger, K. Zaghib, C. Julien, J. Power Sources 240 (2013) 267–272.
[37] J.-G. Wang, Y. Yang, Z.-H. Huang, F. Kang, J. Power Sources 204 (2012) 236–243.
[38] H. Jiang, J. Ma, C. Li, J. Mater. Chem. 22 (2012) 16939–16942.
[39] P. Li, Y. Yang, E. Shi, Q. Shen, Y. Shang, S. Wu, J. Wei, K. Wang, H. Zhu, Q. Yuan, Acs Appl Mater Inter 6 (2014) 5228–5234.
[40] K. Ghosh, C.Y. Yue, M.M. Sk, R.K. Jena, Acs Appl Mater Inter 9 (2017) 15350–15363.
[41] X. Fan, X. Wang, G. Li, A. Yu, Z. Chen, J. Power Sources 326 (2016) 357–364.
[42] H. Xu, X. Hu, H. Yang, Y. Sun, C. Hu, Y. Huang, Adv Energy Mater 5 (2015) 1401882–1401888.
[43] X. Lu, M. Yu, G. Wang, T. Zhai, S. Xie, Y. Ling, Y. Tong, Y. Li, Adv. Mater. 25 (2013) 267–272.
[44] M. Cakici, R.R. Kakarla, F. Alonso-Marroquin, Chem. Eng. J. 309 (2017) 151–158.
[45] L. Yu, G. Zhang, C. Yuan, X.W.D. Lou, Chem. Commun. 49 (2013) 137–139.
[46] S.-I. Kim, J.-H. Kang, S.-W. Kim, J.-H. Jang, Nanomater. Energy 39 (2017) 639–646.
[47] M. Shi, L. Zhao, X. Song, J. Liu, P. Zhang, L. Gao, Acs Appl Mater Inter 8 (2016) 32460–32467.
[48] X. Lang, A. Hirata, T. Fujita, M. Chen, Nat. Nanotechnol. 6 (2011) 232–236.
[49] Y. He, W. Chen, X. Li, Z. Zhang, J. Fu, C. Zhao, E. Xie, ACS Nano 7 (2012) 174–182.
[50] Y.X. Xu, Z.Y. Lin, X. Zhong, X.Q. Huang, N.O. Weiss, Y. Huang, X.F. Duan, Nat. Commun. 5 (2014) 4554–4561.
[51] X. Cao, Y. Shi, W. Shi, G. Lu, X. Huang, Q. Yan, Q. Zhang, H. Zhang, Small 7 (2011) 3163–3168.
[52] C. Xiong, T. Li, A. Dang, T. Zhao, H. Li, H. Lv, J. Power Sources 306 (2016) 602–610.
[53] L. Pan, G. Yu, D. Zhai, H.R. Lee, W. Zhao, N. Liu, H. Wang, B.C.-K. Tee, Y. Shi, Y. Cui, Proc. Natl. Acad. Sci. Unit. States Am. 109 (2012) 9287–9292.
[54] M.D. Stoller, R.S. Ruoff, Energy Environ. Sci. 3 (2010) 1294–1301.
[55] A. Laheäär, P. Przygocki, Q. Abbas, F. Béguin, Electrochem. Commun. 60 (2015) 21–25.
[56] T. Brousse, D. Bélanger, J.W. Long, J. Electrochem. Soc. 162 (2015) A5185–A5189.
[57] Y. Gogotsi, P. Simon, Science 334 (2011) 917–918.
[58] Y. Hou, Y. Cheng, T. Hobson, J. Liu, Nano Lett. 10 (2010) 2727–2733.
[59] S. Devaraj, N. Munichandraiah, J. Phys. Chem. C 112 (2008) 4406–4417.
[60] D. Guo, Y. Luo, X. Yu, Q. Li, T. Wang, Nanomater. Energy 8 (2014) 174–182.
[61] R.V. Salvatierra, L.G. Moura, M.M. Oliveira, M.A. Pimenta, A.J. Zarbin, J. Raman Spectrosc. 43 (2012) 1094–1100.
[62] T. Gao, H. Fjellvåg, P. Norby, Anal. Chim. Acta 648 (2009) 235–239.

[63] E. Widjaja, J.T. Sampanthar, Anal. Chim. Acta 585 (2007) 241–245.

[64] J.M. Jeong, B.G. Choi, S.C. Lee, K.G. Lee, S.J. Chang, Y.K. Han, Y.B. Lee, H.U. Lee, S. Kwon, G. Lee, Adv. Mater. 25 (2013) 6250–6255.

[65] X.-F. Lu, X.-Y. Chen, W. Zhou, Y.-X. Tong, G.-R. Li, Acs Appl Mater Inter 7 (2015) 14843–14850.

[66] V. Augustyn, J. Come, M.A. Lowe, J.W. Kim, P.-L. Taberna, S.H. Tolbert, H.D. Abruña, P. Simon, B. Dunn, Nat. Mater. 12 (2013) 518–522.

[67] L. Zhu, Y. Liu, C. Su, W. Zhou, M. Liu, Z. Shao, Angew. Chem. 128 (2016) 9728–9731.

[68] J.T. Mefford, W.G. Hardin, S. Dai, K.P. Johnston, K.J. Stevenson, Nat. Mater. 13 (2014) 726–732.

[69] N. Jabeen, A. Hussain, Q. Xia, S. Sun, J. Zhu, H. Xia, Adv. Mater. 29 (2017) 1700804–1700812.

[70] A.E. Fischer, K.A. Pettigrew, D.R. Rolison, R.M. Stroud, J.W. Long, Nano Lett. 7 (2007) 281–286.

[71] R. Liu, J. Duay, S.B. Lee, ACS Nano 4 (2010) 4299–4307.

[72] Y. Liu, Y. Qiao, W. Zhang, H. Xu, Z. Li, Y. Shen, L. Yuan, X. Hu, X. Dai, Y. Huang, Nanomater. Energy 5 (2014) 97–104.

[73] J. Chang, M. Jin, F. Yao, T.H. Kim, V.T. Le, H. Yue, F. Gunes, B. Li, A. Ghosh, S. Xie, Adv. Funct. Mater. 23 (2013) 5074–5083.

[74] P.-J. Hung, K.-H. Chang, Y.-F. Lee, C.-C. Hu, K.-M. Lin, Electrochim. Acta 55 (2010) 6015–6021.

[75] K. Honda, T.N. Rao, D. Tryk, A. Fujishima, M. Watanabe, K. Yasui, H. Masuda, J. Electrochem. Soc. 147 (2000) 659–664.